ICAS 2020 SHANGHAI
International Council of the Aeronautical Sciences
32nd Congress of the International Council of the Aeronautical Sciences
September 6-10, 2021
Pudong Shangri-La, Shanghai, China

AN INTEGRATED METHOD FOR ACCURATE IDENTIFICATION AND DYNAMIC MONITORING OF BUILDINGS IN AERODROME OBSTACLE FREE SPACE

Kuang Tong, Yang Song, Xiangfen Kong, Kaiwen Zhang, Zijian Chen

Civil Aviation University of China

Abstract

This paper presents an integrated method for accurate identification and dynamic monitoring of Aerodrome Obstacle Free Space (AOFS) buildings based on Digital Surface Model (DSM) and data of Point of Interest (POI). Specifically, the first step is to construct minimum bounding rectangles (MBR) of ultra-high or dynamic grid cells by time-series DSMs based on time-series stereo pairs. Secondly, the height, height changed rate, name, and other features of ultra-high or dynamic buildings are automatically extracted combined with the function of POI range search. Finally, in order to realize irregular dynamic monitoring for buildings in AOFS, the change rate of building elevation is used as the basis to estimate the next time interval of dynamic monitoring. In the meantime, Shenzhen Baoan International Airport is taken as the study area to evaluate the approach proposed in this paper. The results show that the accuracy of this integrated approach in building identification and monitoring only depends on the accuracy of DSMs, and there is no restriction on the data source of DSMs. Moreover, only identifying and monitoring ultra-high and dynamic buildings can reduce data redundancy due to repeatedly extract all buildings. Irregular dynamic monitoring based on the rate of elevation change of potentially dangerous buildings can further reduce data costs while ensuring AOFS's safety in the monitoring interval.

Keywords: aerodrome obstacle free space (AOFS), building height, identification and monitoring, point of interest (POI), digital surface model (DSM)

1. Introduction

AOFS is a spatial area around the airport that restricts landforms and ground objects' height to ensure the safety of taking off, landing, and going around [1,2]. In recent years, with the acceleration of urbanization and the development of the airport economic zone, the contradiction between the security of AOFS and the expansion of urban construction land becomes increasingly severe [3-5]. Since the quality of AOFS directly affects flight safety, the accurate identification and dynamic monitoring of over-high buildings/potentially dangerous buildings in AOFS based on high-resolution remote sensing data becomes an important research direction of intelligent airport.

With the development of sensors, artificial intelligence, and other technologies, Light Detection and Ranging (LiDAR) point cloud, space-borne optic remote sensing imagery, and Synthetic Aperture Radar (SAR) imagery are widely used in the identification and monitoring of city buildings [6-14]. Since the influence of airport airspace restrictions and "non-stop flight construction" policies, LiDAR has less application in monitoring buildings in AOFS. Space-borne optic remote sensing imagery and SAR based on space-borne satellite imagery are different in height extraction because of different imaging principles. They can be roughly divided into shadow altimetry and stereo pairs method. However, the shadow altimetry method is based on single optic remote sensing imagery, single SAR imagery, single optic remote sensing imagery, and single SAR imagery combined by establishing the linear relationship between shadow lengths and building heights [15-17]. Because of the shadow altimetry method needs to determine the shadow length of buildings in advance by classification, threshold classification and edge detection, it is difficult to identify and extract the height of buildings automatically in large area [18-22]. In the meantime, the DSM generated based on the optical remote sensing or SAR stereo pairs and combined with the existing geographic database can realize the automatic identification and height extraction of large-area buildings [23].

Because of the high precision and cost, the approaches based on SAR stereo pairs is often used to monitor a single important building or infrastructure [24]. However, it is challenging to be popularized in the large-scale dynamic monitoring of buildings. The other method based on optic remote sensing stereo pairs has insufficient data cost and high automation level. However, this method often lacks the key parameters of optical remote-sensing satellite and is easily affected by weather, which leads to low horizontal geometric positioning and elevation accuracy in DSM.
In conclusion, on the one hand, the shadow altimetry and stereo pairs method have the problems of low automation level and high data cost in large area building identification and monitoring. On the other hand, both methods separate building identification from height monitoring. Specifically, each monitoring needs to repeatedly determine the contour or shadow length of all buildings, and then get the height of all buildings through matching or inversion. In order to realize accurate identification and dynamic monitoring for buildings in AOFS in a low cost and intuitive way, based on time-series stereo pairs and POI data, this paper proposes an integrated approach for recognizing and monitoring buildings. Firstly, the approach realizes the judgment of whether every grid cell's attribute is ultra-high or dynamic based on DSMs of AOFS generated by two pairs of Ziyuan3-02 optical remote sensing stereo pairs at arbitrary time intervals. Then, we design an algorithm to combine the same attribute of grid cells to generate the MBRs. Combined with the Baidu Maps' range retrieval function, the automatic identification and hierarchical safety management of the ultra-high or dynamic buildings [25]. Finally, the interval of irregular dynamic monitoring is adjusted according to the maximum height changed rate of dynamic buildings. It also realizes the accurate identification and dynamic monitoring for buildings in AOFS with lower data cost, higher automation, and high integration.

2. Study Area and Data

2.1 Review of the Study Area

This paper selects Shenzhen Baoan International Airport (Figure 1) as the study area. It locates in China's Shenzhen Baoan district and belongs to low mountain hilly coastal zone and subtropical marine climate, with an average temperature of 22 °C, annual rainfall of 1.93 m. The geographic coordinates are E113°49', N22°36', and the airport elevation is 3.96 m, 32 km away from Shenzhen city.

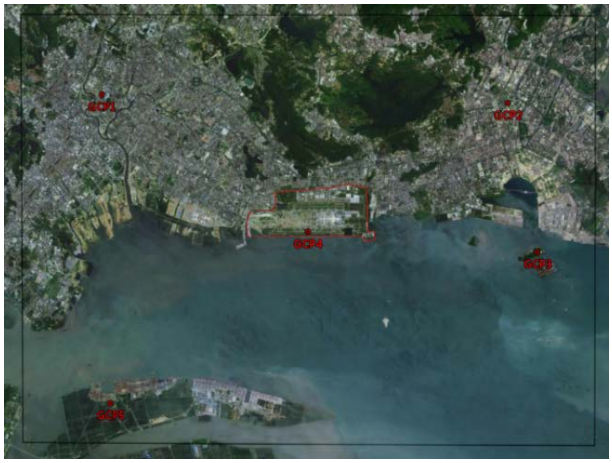

Figure 1 – Review of the study area and AOFS. The red dotted line is the study area.

2.2 Data Sources

Optical remote sensing satellite data used in this paper are two pairs of three-line array stereo pairs of the Ziyuan3, no. 02 satellites (abbreviated as Ziyuan3-02) taken on March 29, 2019, and April 23, 2020, respectively. Airport's headroom parameters are derived from "International Civil Aviation Convention Annex 14-Airport Design and Operation". The POI data comes from Baidu Maps JavaScript API v2.0. Thirty-five ground control points (GCPs) are used for geometric correction. In addition, data of airport surrounding construction and planning are used for building identification and floor height verification. All data are shown in Table 1.

Table 1 Data and its descriptions.

Data	Description	Date	Source
Ziyuan3-02	Face viewed full-color 2.1m	2019-3-29	Institute of Remote Sensing and Digital Earth Chinese Academy Sciences
	Front and rear viewed 22° full-color 2.5m	2020-4-23	
POI data	NA	NA	Baidu Maps JavaScript API V2.0
GCPs	There are thirty-five with five ground control points and thirty checking points	2020-10-03	Artificial measurement

3. Methodology

3.1 Flow Chart of the Integrated Method

Accurate identification and dynamic monitoring of buildings in AOFS usually involve three aspects, consisting of determining the restricted height of buildings in unique positions of a cleared area, extracting the height of buildings, and safety evaluation and management of dangerous or potentially dangerous buildings. This paper's key idea is to realize accurate identification and dynamic monitoring of ultra-high or dynamical buildings in AOFS based on DSMs generated by ziyuan3-02 stereo pairs in two periods and POI data. Firstly, based on the airport grade and runway parameters, a parametrized and mathematical model of obstacle limitation surfaces (OLS) in AOFS is constructed. The grid cell's size is twice the relative positioning error of the DSMs in the horizontal direction to ensure that each grid cell at different from timings represents or belongs to the same geographic entity. Subsequently, twice the relative height error of DSMs in the vertical direction is used as the threshold for judging whether each grid cell is static or dynamic. Furthermore, we design an algorithm for combining grid cells with the same attribute to generate MBRs of buildings, combined with the function of POI range retrieval to realize buildings' accurate identification. Finally, the identified buildings are divided into three categories, consisting of dangerous buildings, potentially dangerous buildings, and safe buildings for hierarchical safety management. The interval of irregular dynamic monitoring is adjusted according to the maximum height changed rate of potentially dangerous buildings, and realize the accurate identification and dynamic monitoring for buildings in AOFS with lower data cost, higher automation, and high integration (Figure 2).

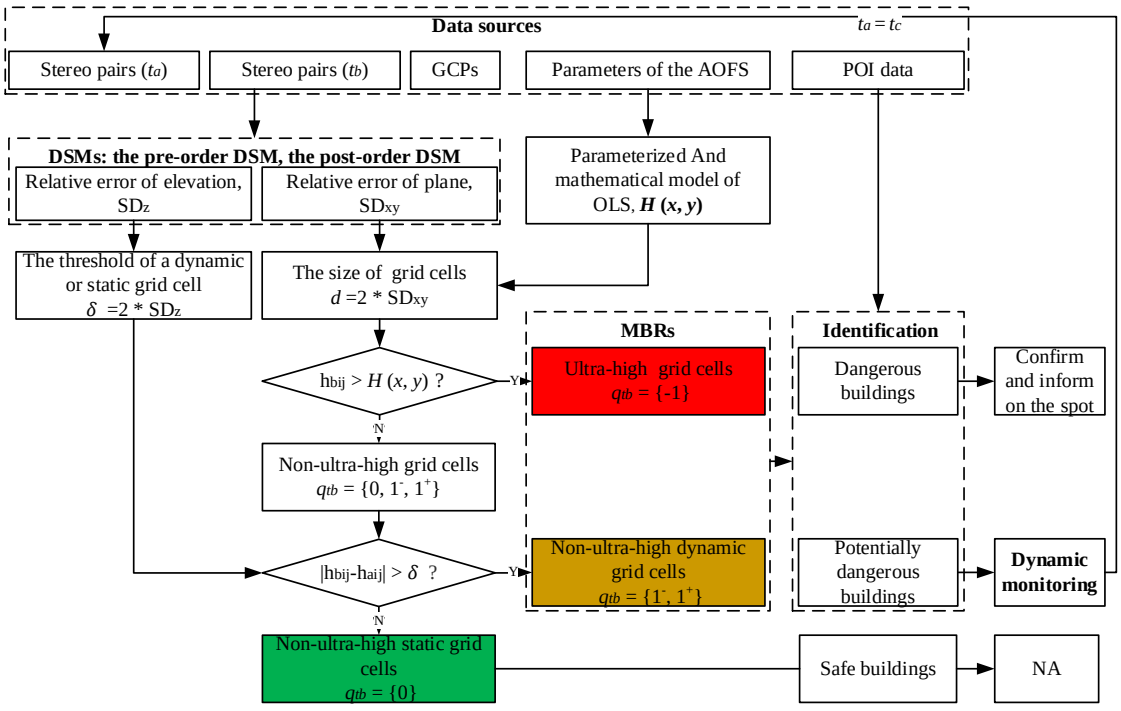

Figure 2 – Flow chart of the integrated method of accurate identification and dynamic monitoring.

3.2 Parameterized and Mathematical Model of Obstacle Limitation Surfaces

Firstly, a mathematical model of OLS in AOFS is constructed in the parameterized way [26,27]. The end and side clearance area restrictions are provided in Appendix Table A1 and A2. The height of OLS at any position ($H(x,y)$), shown in Figure 3, presented in a piecewise function. It can be divided into D_1, D_2, D_3, D_4, D_5, D_6, and D_7 seven parts, of which the study area in this paper is in D_2 and D_4 two parts. Five parts of D_1, D_3, D_5, D_6, and D_7 are in Appendix Table A3.

$$H(x,y) = H_n, (x,y) \in D_2 \cup D_4. \quad (1)$$

Where $H(x,y)$ is the restricted height of the obstacle at any position in AOFS.

The parameterized and mathematical model of OLS in AOFS is ground through vertical mapping, as shown in Figure 3. To ensure that the same grid cell represents the same building entity in the first and second sequences DSM, the grid cell size (d) is twice the plane relative error.

$$d = 2 * SD_{xy}, SD_{xy} = \sqrt{\frac{\sum_{i=1}^{n}(\varepsilon_i^{xy} - ME)^2}{n}}, ME = \sum_{i=1}^{n}\frac{\varepsilon_i^{xy}}{n}. \quad (2)$$

Where ε_i^{xy} is the difference between DSMs and checking points in a plane direction; n is the number of checking points.

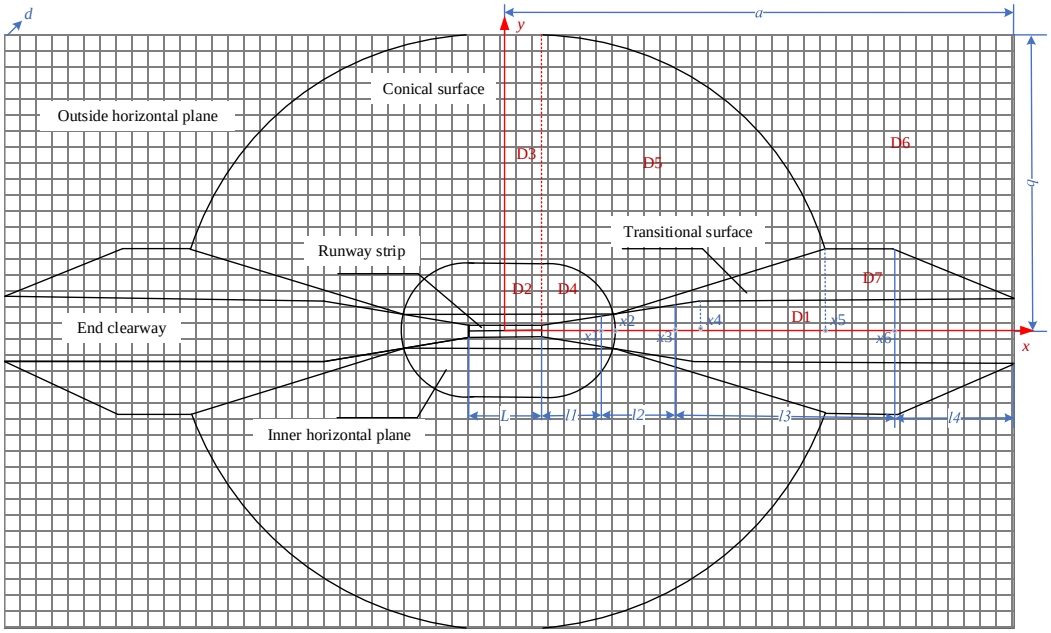

Figure 3 – Parameterized and mathematical model of obstacle limitation surfaces.

3.3 Automatic Identification for Buildings

Based on the size relationship between each grid cell height (H_{bij}) of the DSM in the t_b period (abbreviated as post-order DSM) and the limit height ($H(x,y)$) of each grid cell in AOFS, the post-order DSM is divided into two categories, consisting of ultra-high grid cell and non-ultra-high grid cell (Figure 4(i)):

The grid cell is an ultra-high grid (represented by -1) when $H_{bij} \geq H(x,y)$, where the elevation value of each grid cell in the post-order DSM is H_{bij}.

Subsequently, combining with the DSM in the t_a period (abbreviated as pre-order DSM) judges the dynamic or static attributes of remaining non-ultra-high grid cells in post-order DSM (Figure 4(ii)). The grid cell is static (represented by 0) when $|\Delta H_{ij}| \leq \delta$; else if $|\Delta H_{ij}| > \delta$ and $\Delta H_{ij} > 0$, the grid cell is dynamically decreased (represented by 1^+); else if $|\Delta H_{ij}| > \delta$ and $\Delta H_{ij} < 0$, the grid cell is dynamically increased (represented by 1^-). The elevation difference of each grid cell between the post-order DSM and the pre-order DSM is represented by ΔH_{ij} ($\Delta H_{ij} = h_{bij} - h_{aij}$), δ represents the threshold of a dynamic or static grid cell.

$$\delta = 2 * SD_z, SD_z = \sqrt{\frac{\sum_{i=1}^{n}(\varepsilon_i^z - ME)^2}{n}}, ME = \sum_{i=1}^{n}\frac{\varepsilon_i^z}{n}. \quad (3)$$

Where ε_i^z is the difference between DSMs and the checkpoints in a vertical direction; n is the number of checking points.

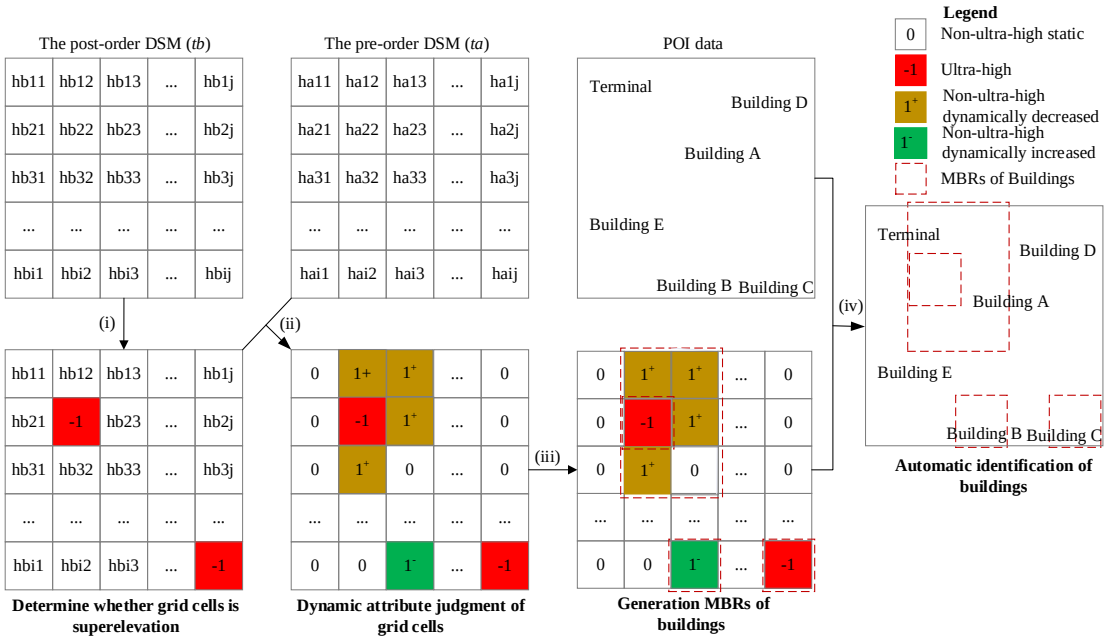

Figure 4 – The algorithm of automatic extraction and identification of buildings.

Next, based on ultra-high or dynamic grid cells' attribute values, an algorithm that combines grid cells with the same attribute into MBRs is designed in this paper (Figure 4(iii)). The algorithm idea presents as follows.

1. Creating single-column MBRs ($n, q, j_{\min}, j_{\max}, i_{\min}, i_{\max}$) by column. Create a single, consecutive MBR with the same dynamic or static attribute of grid cells column by column, and attributes include number n =1,2,...; dynamic and static attribute $q = \{-1, 1^-, 1^+\}$, which respectively represents ultra-high, non-ultra-high dynamically increased and non-ultra-high dynamically decrease; starting column is $j_{\min}$; ending column is $j_{\max}$; starting line is $i_{\min}$; ending line is $i_{\max}$;
2. Merge single-column MBRs by column into multi-columns MBRs ($n, q, j_{\min}, j_{\max}, i_{\min}, i_{\max}$). Start from the first single-column MBR and merge by a column, if the q values of two adjacent columns MBR and MBR' are the same and $[i_{\min}+1, i_{\max}+1]_{\text{MBR}} \cap [i_{\min}+1, i_{\max}+1]_{\text{MBR}'} \neq \emptyset$, single-column MBRs are merged into multi-columns MBRs. At the same time, update the values of the starting column and the ending column;
3. Merge multi-columns MBRs by row into building MBRs ($n, q, j_{\min}, j_{\max}, i_{\min}, i_{\max}$). Start from the first multi-columns MBR and merge by row, if the q values of two adjacent columns MBR and MBR'' are the same and $[j_{\min}+1, j_{\max}+1]_{\text{MBR}} \cap [j_{\min}+1, j_{\max}+1]_{\text{MBR}''} \neq \emptyset$, multi-columns MBRs are merged into building MBRs. At the same time, update the values of building MBRs;

   Example: As shown in Figure 5 (a), the first step of the algorithm generates six single-column MBRs, there are zero single-column MBR in the first column, the second column has three single-column MBRs (MBR_1 (1, 1^+, 2, 2, 1, 1), MBR_2 (2, -1 , 2, 2, 2), MBR_3 (3, 1^+, 2, 2, 3, 3)), the third column has two single-column MBRs (MBR_4(4, 1^+, 3, 3, 1, 2) , MBR_5 (5, 1^-, 3, 3, 1, 1)), and the fourth column has one single-column MBR (MBR_6 (6, -1, *j*, *j*, *i*, *i*)); in the second step of the algorithm (Figure 5 (b)), six single-column MBRs are merged into five multi-columns MBRs by column, in which the merge of MBR_1 and MBR_4 make the values of MBR_1 (1, 1^+, 2, 2, 1, 1) into MBR_1 (1, 1^+, 2, 3, 1, 2), the merge of MBR_3 and MBR_4 makes the values of MBR_3 (3, 1^+, 2, 2, 3, 3) into MBR_3 (3,1^+, 2, 3, 1, 3); The third step (Figure 5 (c)) of the algorithm finally get four building MBRs, that the merge of MBR_1 and MBR_3 makes the values of MBR_1 (1, 1^+, 2, 2, 1, 1) into MBR_1 (1, 1^+, 2, 3, 1, 3), that is, three single-column MBRs (MBR_1, MBR_3, and MBR_4) are merged into one building MBR.

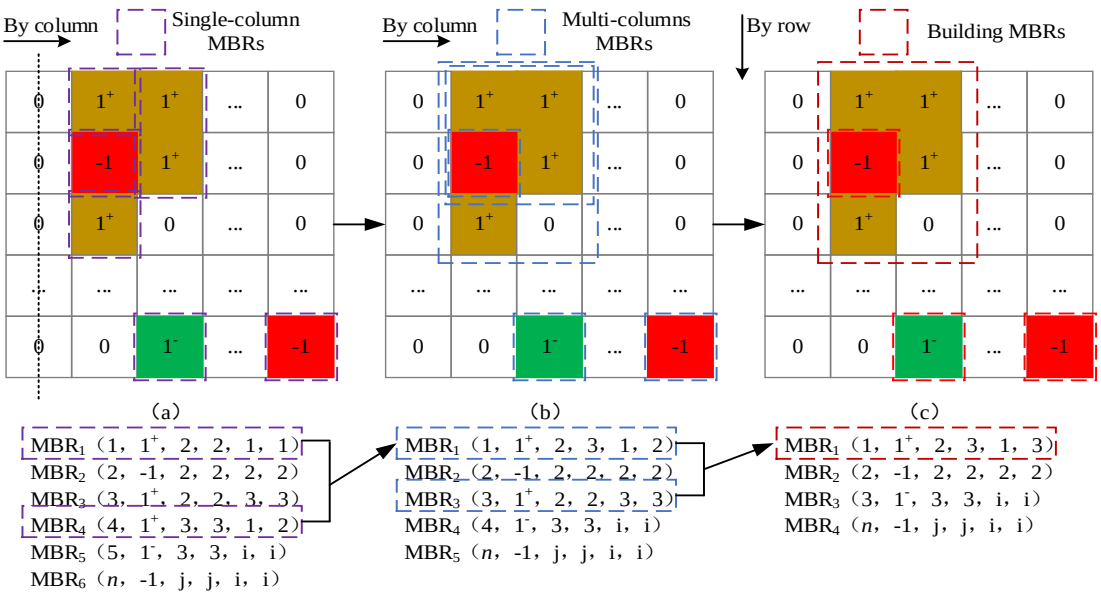

Figure 5 – Grid cells generate building MBRs.

4. Use POI data to identify building MBRs ($n, q, j_{\min}, j_{\max}, i_{\min}, i_{\max}$). Building MBRs in step 3 can only determine each ultra-high or non-ultra-high dynamic building's location and range. However, they lack detailed information, such as the name and the area of each ultra-high and non-ultra-high dynamic buildings. In this paper, POI range retrieval of building MBRs to realize the automatic extraction of properties such as name, area, and other properties of the ultra-high and non-ultra-high dynamic buildings (Figure 4(iv)). Among them, three parameters (Table 2) of the retrieval center point ($O(x, y)$), the length of the rectangular search box (a), and the width of the rectangular search box (b) required for the POI range retrieval can be directly determined by attribute values of building MBRs (Eq. (4) and Eq. (5)).

Table 2 The code of POI range retrieval based on Baidu Maps API V2.0.

Input: $O(x, y)$[1], a, b
Output: $name$

```
int x, y;
double a, b;
private void boundSearch (int page) {
   PoiBoundSearchOption boundSearchOption = new PoiBoundSearchOption (); // southwest coordinate
   LatLng southwest = new LatLng (x – a/2, y – b/2); // northeast coordinate
   LatLng northeast = new LatLng (x + a/2, y + b/2); // set POI retrieval range
   LatLngBounds bounds = new LatLngBounds.Builder().
   include(southwest). include(northeast). build ();
   boundSearchOption.bound(bounds); // search key word "architecture"
   boundSearchOption.keyword(editSearchKeyEt.getText(). toString ());
   boundSearchOption.pageNum(page); // start POI range retrieval request
   poiSearch.searchInBound(boundSearchOption);
   return;}
```

$$\mathrm{b} = (\mathrm{i}_{\max}\text{-}\mathrm{i}_{\min})*\mathrm{d}x = \left[\frac{(j_{\max}-j_{\min})}{2}\right], y = \left[\frac{(i_{\max}-i_{\min})}{2}\right], \quad (4)$$

$$\mathrm{b} = (\mathrm{i}_{\max}\text{-}\mathrm{i}_{\min})*\mathrm{d}a = (j_{\max} - j_{\min}) * d, b = (i_{\max} - i_{\min}) * d. \quad (5)$$

1 Here, to simplify the code using plane coordinates, x and y need to be converted into geographic coordinates in actual use.

3.4 Dynamic Monitoring for Buildings

In order to realize the dynamic monitoring for ultra-high or non-ultra-high dynamic buildings in AOFS, based on the change of q value at current time, buildings are divided into three categories of danger, potential danger and safety, and carried out hierarchical safety management (Table 3).

- Safe buildings: There is no need for any measures for the four types of safe buildings. Specifically, they do not affect the safety of the AOFS.
- Dangerous buildings: The situation of the four dangerous buildings should be confirmed on the spot and informed by the relevant planning department. In other words, the impact of the dangerous buildings on the safety of the AOFS should be removed in time.
- Potentially dangerous buildings: Dynamic monitoring is carried out for three kinds of potentially dangerous buildings. The next monitoring time (t_c) is estimated according to the potentially dangerous building that may become a dangerous building as soon as possible.

$$t_c = t_b + \left[\frac{\min\{t_n\}}{\mathrm{T}}\right] * \mathrm{T}, \tag{6}$$

$$t_n = \frac{H_{bij}}{S_{bij}},\ H_{bij} = \min\{H(x,\ y) - h_{bij}\},$$

$$S_{bij} = \begin{cases} \max\left\{\frac{(h_{bij}+h_{aij})}{(t_b-t_a)}\right\} & q \in \{1^- \to 1^+\} \\ \max\left\{\frac{(h_{bij}-h_{aij})}{(t_b-t_a)}\right\}, & q \in \{1^+ \to 1^+,\ 0 \to 1^+\} \end{cases}. \tag{7}$$

Where t_n is the time that each potentially dangerous building become a dangerous building, it equal to the minimum value of the grid cell contained in each potentially dangerous building at the current moment (t_b) distance from OLS (H_{bij}) divided by the maximum elevation change rate of grid cells (S_{bij}) during the monitoring interval ($t_a \to t_b$). t_a and t_b are two adjacent dynamic monitoring moments. The revisit period of the Ziyuan3-02 satellite is T (T = 5 d).

Table 3 Graded safety management of buildings in AOFS.

$q_{t_a \to t_b}$	Category of buildings	Management measures
$-1 \to 1^-;\ 1^- \to 1^-;$ $1^+ \to 1^-;\ 0 \to 1^-.$	Safe buildings	NA
$-1 \to -1;1^- \to -1;$ $1^+ \to -1;\ 0 \to -1.$	Dangerous buildings	Confirm and inform on the spot
$1^- \to 1^+;1^+ \to 1^+;$ $0 \to 1^+.$	Potentially dangerous buildings	Dynamic monitoring

4. Results and Discussion

4.1 Accuracy Evaluation of DSMs from Ziyuan3-02 Stereo Pairs

In order to realize further integration of the accurate identification and dynamic monitoring of buildings based on DSMs by time-series stereo pairs, this paper uses the Free and Open Source Software for Geospatial Digital Automatic Terrain Extractor (FOSS4G DATE) tool to process time-series stereo pairs [28], in which the DSM generated by the stereo pairs in the tb (2020-4-23) period is shown in Figure 6. Plane and elevation adjustment results of DSMs are shown in Table 4.

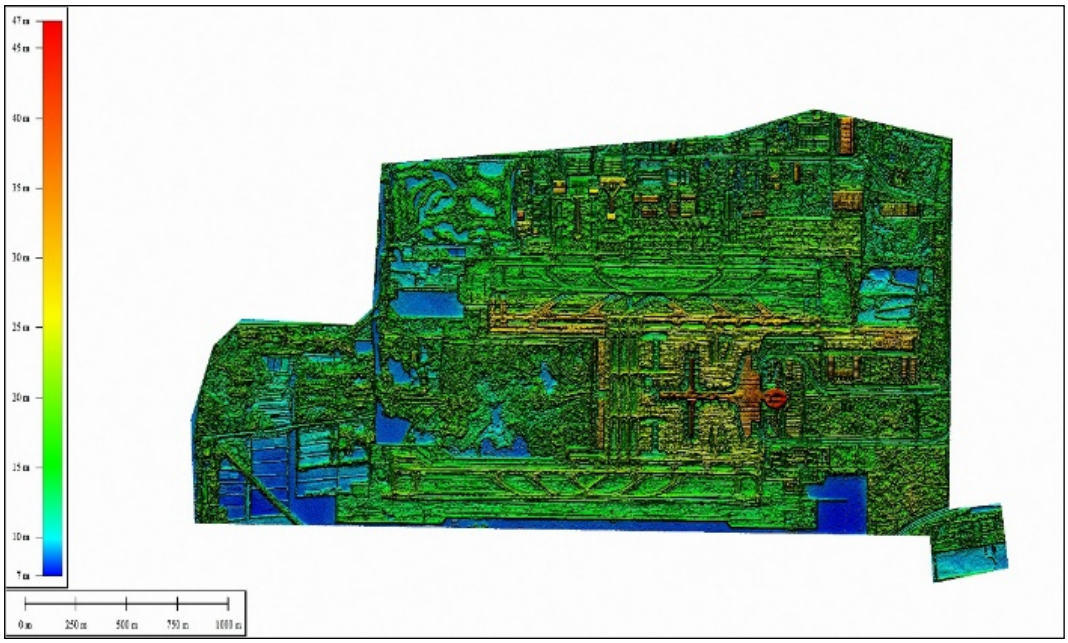

Figure 6 – The DSM of the study area at t_b (2020-4-23) period (6 m * 6 m).

From Table 4, the standard plane deviations of the DSMs in the two periods are 2.87 m and 2.63 m, respectively. It is revealed in the table that the grid cell size of DSMs in this paper is reasonable to set as 6 m. Elevation standard deviations are 1.62 m and 1.58 m, respectively. The δ value can realize floor change monitoring (floor height is generally 3 m). It can be proved that this paper's grid dynamic change threshold is reasonable.

Table 4 Adjustment results of DSMs.

Date of DSMs	Description of precision	Plane (/m)	Elevation (/m)
2019-3-29	The range of Residual error	1.12 ~ 8.36	0.38 ~ 8.90
$(t_a \mathrm{t_a})$	Root Mean Square Error (RMSE)	2.87	1.62
2020-4-23	The range of Residual error	0.98 ~ 9.34	0.72 ~ 8.78
$(t_b \mathrm{t_b})$	Root Mean Square Error (RMSE)	2.63	1.58

Table 5 Attribute values of building MBRs.

n	q	$j_{\min}$	$j_{\max}$	$i_{\min}$	$i_{\max}$	$name$
1	1^+	-690	-725	-61	-77	Null
2	1^+	184	198	214	219	Badminton venue of Shenzhen Airlines headquarters
3	1^+	175	181	186	198	B4 air service building of Shenzhen aviation base
4	1^+	152	158	136	142	Null
5	1^+	348	344	203	211	Aviation oil building of Shenzhen Airport
6	1^+	345	342	188	197	Shenzhen Dewei International Freight Forwarding
7	1^+	346	357	133	140	Shunfeng aviation building; South China transfer center

4.2 The Feasibility of Building Identification

According to the comparison of DSMs grid by the grid in the two periods, the changes of grid cells attributes (Figure 8) are compared with the existing planning data in the study area (seven new high-rise buildings, two single building demolition, one new single floor building, one lake engineering). It can be seen that seven areas are dynamic increased and no one area is ultra-high or dynamic decreased (Table 5). All dynamic buildings' identification accuracy is 64%, and potentially dangerous buildings' identification accuracy is 100%. This paper's integrated approach can realize the accurate identification of dynamic building with floor change greater than one floor.

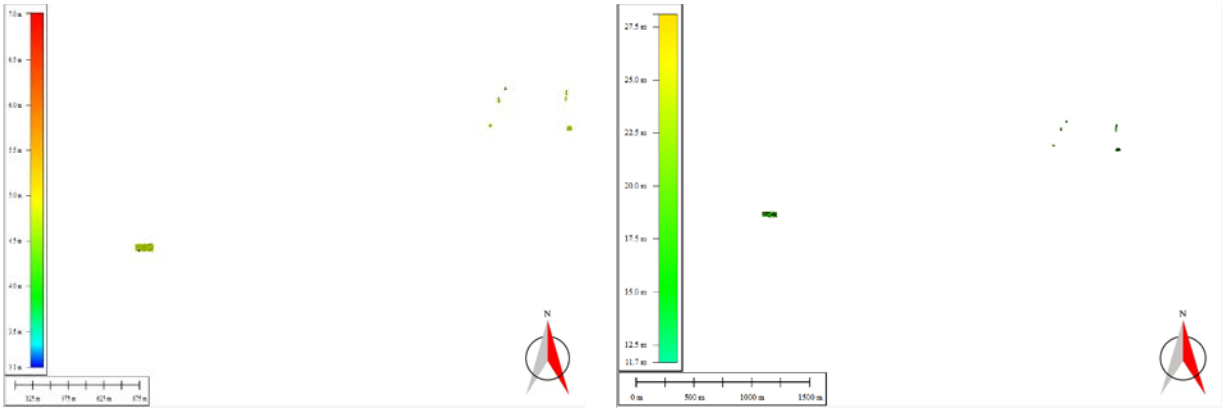

(a) 3.01 m ≤ $h_{bij} - h_{aij}$ ≤ 7.01 m (b) 11.68 m ≤ h_{bij} ≤ 27.10 m

Figure 7 – The elevation change value of MBRs and the elevation of MBRs at t_b (2020-4-23) period.

Based on Baidu Maps API, we perform POI range retrieval on the MBRs of dangerous or potentially dangerous buildings and superimpose the search results with the vector map (Figure 8). The following results can be got.

Figure 8 – Building identification using POI range retrieval.

1. Five of the seven names of building MBRs can be automatically identified (two in Figure 8(b), three in Figure 8(c)). However, one building name in Figure 8(a) and Figure 8(b) cannot be automatically identified. The reason is that the POI data based on the Baidu Maps API are incomplete.
2. Building MBR_7 recognizes two building names because the horizontal error of DSM data itself leads to the inevitable intersection between buildings MBRs which are close to each other, therefore, the rationality of building MBRs instead of building accurate contour is verified.
3. As shown in Figure 8, all building MBRs are generally more extensive than the outlines of buildings in digital line graphics (DLG). The offset in the y-axis direction is more significant than that in the x-axis direction. It verifies that the y-axis of DSM's residual error is greater than that of the x-axis in a plane direction.

4.3 The Feasibility of Building Dynamic Monitoring

In this paper, since the buildings in the study area are in the horizontal plane of the AOFS, it can be seen that the value $H(x, y)$ is 45 m by Eq. (1), and the airport elevation is 3.96 m. Meanwhile, Figure

7 reveals that the maximum elevation change (ΔH_{ij}) of the grid cells is 7.01 m (Figure 7(a)). The maximum elevation change rate (S_{bij}) of the grid cells is 0.28 m/d; the value of h_{bij} is 27.10 m (Figure 7(b)). The interval time for the next monitoring is 75 d by Eq. (6) and Eq. (7), which represents the time of next dynamic monitoring (t_c) is July 07, 2020. Through the historical imagery of Google Maps (Figure 9(b)), the building has been completed on July 03, 2020, which shows that the estimation method of irregular dynamic monitoring in this paper is feasible and straightforward. On the one hand, it indicates that the dynamic monitoring method is feasible. On the other hand, it can further reduce the data source's cost by estimating the time interval of irregular dynamic monitoring while ensuring AOFS's safety.

(a) Ziyuan3-02 imagery (2020-4-23) (b) Google Maps historical imagery (2020-7-03)

Figure 9 – The feasibility of dynamic monitoring by using historical imageries of Google Maps.

5. Conclusions

In this paper, firstly, the accuracy of DSMs generated by the Ziyuan3-02 optical remote sensing satellite is evaluated. Then this paper designs an algorithm for combining grid cells with the same attributes into building MBRs and realizes integrating building identification and monitoring combined with POI range searching function based on the plane and elevation errors of DSMs and Baidu Maps API. Moreover, this paper uses Shenzhen Baoan International Airport as the research area to evaluate and verify the feasibility of the integrated method proposed in this paper. According to the study results, the important conclusions can be drawn as follows.

- The method has a lower data cost and redundancy. On the one hand, compared with synthetic aperture radar or LiDAR, Ziyuan3-02 stereo pairs have a lower cost. Meanwhile, the accuracy of Ziyuan3-02 stereo pairs can realize accurate identification and dynamic monitoring on potentially dangerous buildings with floor changes greater than one floor. On the other hand, the method of only identifying and monitoring ultra-high or dynamic buildings can not only ensure the safety of AOFS, but also reduce the high data cost caused by repeatedly identifying and regular monitoring all buildings.
- The method has a higher openness and integration. Since the elevation changes of grid cells in DSMs at different times are used to realize the identification and monitoring of buildings, the proposed approach's feasibility and accuracy are only related to DSMS's accuracy. There is no restriction on the data sources of DSMs. Moreover, this paper's method is suitable for monitoring and managing buildings in any AOFS because the height model of OLS is parameterized. The integration of this method can be further improved by processing the original remote sensing imagery with an openness tool.

However, since the accuracy of DSMs is not only related to the type of original data (optical satellite stereo pairs, SAR stereo pairs, and LiDAR point cloud) and the accuracy of data itself, but also related to the topography of the study area [29], the size of grid cells and the threshold value of dynamic changes of grid cells mentioned in this method need to be adaptively and dynamically adjusted according to the accuracy of DSMs in water level and elevation direction respectively. In addition, it leads to the low accuracy of identification and monitoring in the area with dense buildings. Moreover, it is difficult to widely popularize this paper's approach because of its low portability.

Appendix: Parameters of AOFS and Heights of OLS in D_1, D_3, D_5, D_6, and D_7 parts.

Table A1 Parameters of end OLS.

The first paragraph			**The second paragraph**			**The third paragraph**			**The fourth paragraph**			**Total length**
Length	Slope	End height	Length	Slope	End height	Length	Slope	End height	Length	Slope	End height	
l_1	k_1	H_1	l_2	k_2	H_2	l_3	k_3	H_3	l_4	k_4	H_4	a

Table A2 Parameters of side OLS.

Transitional surface	**Inner horizontal plane**		**Conical surface**			**Side width of runway centerline**
Slope	Radius	Height	Radius	Slope	Height of the Outside edge	
$1/10$	r_1	H_n	r_2	K'	H_w	b

Table A3 Heights of OLS in D_1, D_3, D_5, D_6, and D_7 parts.

Piecewise function of $H(x,y)$	**Part**	**Piecewise function of $H(x,y)$**	**Part**
$H(x,y)=\begin{cases}0 & 0<x\le L/2\\ k_1(x-L/2) & L/2<x\le x_1\\ H_1+k_2(x-x_1) & x_1<x\le x_3\\ H_2=H_3 & x_3<x\le x_6\\ H_3+k_4(x-x_6) & x_6<x\le a+L/2\end{cases}$	D_1	$H(x,y)=\begin{cases}(y-100)/10 & 0<x\le L/2\\ [y-100-0.15(x-L/2)]/10+k_1(x-L/2) & L/2<x\le x_1\\ [y-100-0.15(x-L/2)]/10+H_1+k_2(x-x_1) & x_1<x\le x_3\\ [y-100-0.15(x-L/2)]/10+H_2 & x_3<x\le x_4\\ (y-1500)/10+H_2 & x_4<x\le x_6\\ (y-1500)/10+H_2+k_4(x-x_6) & x_6<x\le a+L/2\end{cases}$	D_7
$H(x,y)=H_n+k'(y-r_1)$	D_3		
$H(x,y)=H_n+k'\lvert\sqrt{(x-L/2)^2+y^2}-r_1\rvert$	D_5	$H(x,y)=H_w$	D_6

References

[1] ICAO. International standards and recommended practices: aerodromes; annex 14 to the convention on international civil aviation; volume I: aerodrome design and operations, *Montreal*, 1999.

[2] Kim D, Kim W. A case study on application of obstacle limitation criteria for specific conditions of airports. *Journal of the Korean Society for Aviation and Aeronautics*, Vol. 24, No. 2, pp 25-30, 2016.

[3] Liebe U, Preisendörfer P and Enzler H B. The social acceptance of airport expansion scenarios: A factorial survey experiment, *Transportation Research Part D: Transport and Environment*, Vol. 84, pp 102363, 2020.

[4] Wang D, Gong Z and Yang Z. Design of industrial clusters and optimization of land use in an airport economic zone. *Land Use Policy*, Vol. 77, pp 288-297, 2018.

[5] Wei Y, Li H and Yue W. Urban land expansion and regional inequality in transitional China. *Landscape and Urban Planning*, Vol. 163, pp 17-31, 2017.

[6] Liu M, Shao Y, Li R, et al. Method for extraction of airborne LiDAR point cloud buildings based on segmentation. *PLOS ONE*, Vol. 15, No. 5, pp e0232778, 2020.

[7] Wang X and Li P. Extraction of urban building damage using spectral, height and corner information from VHR satellite images and airborne LiDAR data. *ISPRS Journal of Photogrammetry and Remote Sensing*, Vol. 159, pp 322-336, 2020.

[8] Shao Z, Tang P, Wang Z, et al. BRRNet: A fully convolutional neural network for automatic building extraction from high-resolution remote sensing images. *Remote Sensing*, Vol. 12, No.6, pp 1050, 2020.

[9] Li X, Zhou Y, Gong P, et al. Developing a method to estimate building height from Sentinel-1 data. *Remote Sensing of Environment*, Vol. 240, pp 1117055, 2020.

[10] Shiroma G and Lavalle M. Digital terrain, surface, and canopy height models from InSAR backscatter-height histograms. *IEEE Transactions on Geoscience and Remote Sensing*, Vol. 58, No. 6, pp 3754-3777, 2020.

[11] Frantz D, Schug F, Okujeni A, et al. National-scale mapping of building height using Sentinel-1 and Sentinel-2 time series. *Remote Sensing of Environment*, Vol. 252, pp 112128, 2020.

[12] Xu Y, Ma P, Ng E, et al. Fusion of WorldView-2 stereo and multitemporal TerraSAR-X images for building height extraction in urban areas. *IEEE Geoscience and Remote Sensing Letters*, Vol. 12, No. 8, pp 1795-1799, 2015.

[13] Thiele A, Cadario E, Schulz K, et al. Building recognition from multi-aspect high-resolution InSAR data in urban areas. *IEEE Transactions on Geoscience and Remote Sensing*, Vol. 45, No. 11, pp 3583-3593, 2007.

[14] Shi Y, Bamler R, Wang Y, et al. SAR tomography at the limit: Building height reconstruction using only 3–5 TanDEM-X bistatic interferograms. *IEEE Transactions on Geoscience and Remote Sensing*, Vol. 58, No. 11, pp 8026-8037, 2020.

[15] Zeng C, Wang J, Zhan W, et al. An elevation difference model for building height extraction from stereo-image-derived DSMs. *International Journal of Remote Sensing*, Vol. 35, No. 22, pp 7614-7630, 2014.

[16] Liu C, Krylov V, Kane P, et al. IM2ELEVATION: Building height estimation from single-view aerial imagery. *Remote Sensing*, Vol. 12, No. 17, pp 2719, 2020.

[17] Shahzad M, Maurer M, Fraundorfer F, et al. Buildings detection in VHR SAR images using fully convolution neural networks. *IEEE Transactions on Geoscience and Remote Sensing*, Vol. 57, No. 2, pp 1100-1116, 2019.

[18] Chen Y, Tang L, Yang X, et al. Object-based multi-modal convolution neural networks for building extraction using panchromatic and multispectral imagery. *Neurocomputing*, Vol. 386, pp 136-146, 2020.

[19] Ma J, Wu L, Tang X, et al. Building extraction of aerial images by a global and multi-scale encoder-decoder network. *Remote Sensing*, Vol. 12, No. 15, pp 2350, 2020.

[20] Uzar M. Automatic building extraction with multi-sensor data using rule-based classification. *European Journal of Remote Sensing*, Vol. 47, No. 1, pp 1-18, 2014.

[21] Siddiqui F, Teng S, Awrangjeb M, et al. A robust gradient based method for building extraction from LiDAR and photogrammetric imagery. *Sensors*, Vol. 16, No. 7, pp 1110, 2016.

[22] Sun G, Huang H, Weng Q, et al. Combinational shadow index for building shadow extraction in urban areas from Sentinel-2A MSI imagery, *International Journal of Applied Earth Observation and Geoinformation*, Vol. 78, pp 53-65, 2019.

[23] Liasis G, Stavrou S. Satellite images analysis for shadow detection and building height estimation. *ISPRS Journal of Photogrammetry and Remote Sensing*, Vol. 119, pp 437-450, 2016.

[24] Wang W, Xu Y, Ng E, et al. Evaluation of satellite-derived building height extraction by CFD simulations: a case study of neighborhood-scale ventilation in Hong Kong. *Landscape and Urban Planning*, Vol. 170, pp 90-102, 2018.

[25] Li Y, Huang J, Fan M, et al. Personalized query auto-completion for large-scale POI search at Baidu Maps. *ACM Transactions on Asian and Low-Resource Language Information Processing*, Vol. 19, No. 5, pp 1-16, 2020.

[26] Contreras-Alonso M, Ezquerra-Canalejo A, Pérez-Martín E, et al. Environmental assessment of Obstacle Limitation Surfaces (OLS) in airports using geographic information technologies. *PLOS ONE*, Vol. 15, No. 2, pp e0229378, 2020.

[27] Qiao X, Lv S, Li L, et al. Application of DSM in obstacle clearance surveying of aerodrome. *ISPRS - International Archives of the Photogrammetry, Remote Sensing and Spatial Information Sciences*, Vol. XLI-B2, pp 227-233, 2016.

[28] Rita M D, Nascetti A and Crespi M. FOSS4G DATE for DSMs generation from tri-stereo optical satellite images: development and first results. *European Journal of Remote Sensing*, Vol. 51, No. 1, pp 472-485, 2018.

[29] Fratarcangeli F, Murchio G, Rita M D, et al. Digital surface models from ZiYuan-3 triplet: performance evaluation and accuracy assessment. *International Journal of Remote Sensing*, Vol. 37, No. 15, pp 3505-3531, 2016.

Acknowledgments

The Fundamental Research Funds for the Central Universities (No.3122014C001) and The Research and Innovation Fund Project for Postgraduates of the Civil Aviation University of China (No.2020YJS051) are provided the funding for this study.

Contact Author Email Address

K. Tong: 2019152008@cauc.edu.cn
Y. Song: y-song@cauc.edu.cn
X.-F. Kong: xfkong@cauc.edu.cn
K.-W. Zhang: 2019152007@cauc.edu.cn
Z.-J. Chen: 2019152005@cauc.edu.cn

Copyright Statement